Transport in Porous Media (2019) 127:685–709
https://doi.org/10.1007/s11242-018-1220-1

# Modelling Low-Salinity Oil Recovery Mechanisms Using an Ion Dissociation Model

**Z. M. Wilmott[1] · C. J. W. Breward[1] · S. J. Chapman[1]**

Received: 23 April 2018 / Accepted: 10 December 2018 / Published online: 26 December 2018


**Abstract**
Experimental evidence shows that injecting low-salinity water during the oil recovery process can lead to an increase in the amount of oil recovered. Numerous mechanisms have been proposed to explain this effect, and, in recent years, two which have gained notable support are multicomponent ionic exchange (MIE) and pH increase. Both mechanisms involve ion exchange reactions within the thin film of water separating the oil in a reservoir from the clay minerals on the surface of the reservoir rock. Since the reactions occur on the molecular scale, an upscaled model is required in order to accurately determine the dominant mechanism using centimetre-scale experiments. In this paper, we develop the first stages of this upscaling process by modelling the pore-scale motion of an oil slug through a clay pore throat. We use a law-of-mass-action approach to model the exchange reactions occurring on the oil–water and clay–water interfaces in order to derive expressions for the surface charges as functions of the salinity. By balancing the disjoining pressure in the water film with the capillary pressure across the oil–water interface, we derive an expression for the salinity-dependent film thickness. We compare the two mechanisms by modifying an existing model for the velocity of an oil slug through a pore throat. Numerical results show that the velocity increases as the salinity decreases. The percentage increase is larger for the MIE mechanism, suggesting that MIE may be the dominant causal mechanism; however, this will vary depending on the particular clay and oil being studied.

**Keywords** Low-salinity oil recovery · Multicomponent ionic exchange · pH increase · Ion dissociation · Disjoining pressure

## 1 Introduction

Due to the ever-increasing demand for energy, the oil and gas industry is continually developing enhanced oil recovery methods to increase the amount of oil that can be extracted from oil reservoirs. One of these methods, which is particularly appealing due to its ease of imple-

✉ Z. M. Wilmott
wilmott@maths.ox.ac.uk

[1] Mathematical Institute, University of Oxford, Radcliffe Observatory Quarter, Woodstock Road, Oxford OX2 6GG, UK

mentation, is low-salinity waterflooding (LSW), which involves the injection of low-salinity water into an oil reservoir. It has been observed in numerous experiments (Jadhunandan 1990; Ligthelm et al. 2009; RezaeiDoust et al. 2011; Tang and Morrow 1999; Yildiz and Morrow 1996) that using LSW as either a secondary process, in which the low-salinity water is injected into a reservoir saturated with oil, or as a tertiary process, in which low-salinity water is injected after a high-salinity waterflood has been performed, can lead to an increase in the amount of oil recovered; this is known as the low-salinity effect (LSE). In order to simulate a low-salinity injection and to determine whether LSW would be effective in a particular reservoir, it is important to understand the chemical and physical processes causing the LSE. However, due to the complexity of the reactions occurring in an oil reservoir, the dominant mechanism is still under debate.

Over the past couple of decades, a number of mechanisms have been proposed to explain the LSE in a sandstone reservoir, such as fines migration (Tang and Morrow 1999), interfacial tension reduction (McGuire et al. 2005), and wettability alteration (Tang and Morrow 1996). Two proposals which have gathered notable support in recent years are multicomponent ionic exchange (MIE) (Lager et al. 2008) and pH increase (Austad et al. 2010), which both involve the release of oil from the rock surface as the result of ion exchange reactions. Whilst many of the proposed mechanisms are based on interactions which occur at the oil–rock interface, there is also a growing body of work suggesting that the LSE may be due to the build up of a viscoelastic interface in low-salinity water, which stabilises the water-in-oil emulsion in a reservoir (Alvarado et al. 2014a; Moradi et al. 2010; Wang and Alvarado 2012).

Various experimental studies (Austad et al. 2010; Lager et al. 2008; Lee et al. 2010; Ligthelm et al. 2009; Moradi et al. 2010; RezaeiDoust et al. 2011; Tang and Morrow 1999) have been conducted to determine which of these processes is the primary mechanism. Moradi et al. (2010) demonstrate experimentally that decreasing the salinity increases the water-in-oil emulsion stability, supporting the viscoelasticity mechanism; this is consistent with a study conducted by Wang and Alvarado (2012). Hilner et al. (2015) use atomic force microscopy to demonstrate that the electric double layer force contributes to the LSE. They find that the threshold for the low-salinity response fits well with the results from field tests. Mahani et al. (2015) investigate the kinetics of oil detachment from clay minerals attached to a glass surface. They observe a wettability alteration in the low-salinity regime and find that the kinetics are consistent with an electrokinetic ion diffusion mechanism.

Numerous 'core flood' experimental investigations have been performed, in which a sample of reservoir rock containing clay minerals, approximately $10\,\text{cm} \times 4\,\text{cm}^2$, is waterflooded with brine, and the effluent is studied in order to determine the reactions that have taken place within the sample. Lager et al. (2008) perform core flood experiments in which they observe that an increase in pH, or an increase in the number of fines produced, is not consistent across experiments, and determine that these are secondary effects that occur during LSW, rather than the causal mechanism. They conclude that cation exchange on the clay surfaces is the primary cause of the LSE in a sandstone reservoir. Austad et al. (2010) also perform core flood tests and conclude that local changes in pH at the oil–clay interface cause the LSE. They suggest that the reduction in divalent cations, such as $Mg^{2+}$, observed by Lager et al. is due to the precipitation of $Mg(OH)_2$ as a result of the increased pH. Both Lager and Austad conclude that polar compounds must be present in the oil, clay must be present in the porous medium, and that the initial formation water (connate brine) must contain divalent cations.

Whilst these experiments provide us with a useful insight into the requirements for the LSE to be observed, they have a couple of limitations. One of the major issues is that processes which have similar requirements, such as pH increase and MIE, are difficult to distinguish. As there are no theoretical predictions to compare with the experimental results on the core

scale, it is not always clear which process is causing the LSE in a given experiment. Another limitation of core flood experiments is that they do not provide sufficient data to accurately run a reservoir simulation. This is because properties such as porosity, clay content, oil composition, and brine composition vary significantly over a reservoir, and to obtain enough data points for an accurate representation of the reservoir to use in a waterflood simulator would require more core flood experiments than is practical.

One way of overcoming these limitations is to derive mathematical models for the different mechanisms, in particular to 'scale up' the effect of each process from the molecular scale to the core scale. As core-scale experiments are more easily performed than molecular-scale experiments, predictions made using the core-scale mathematical models can be easily tested; thus, the dominant process causing the LSE can be more accurately determined. Additionally, with a core-scale model, given the results of a few core-scale experiments, the effect of LSW on other parts of the reservoir can be extrapolated from these data by fitting the relevant parameters. Hence, a core-scale model of LSW would be useful for reservoir-scale simulation.

In this paper, we consider the first stages of this process by deriving pore-scale models for the MIE and pH increase mechanisms, and a similar approach may be used to mathematically model alternative low-salinity mechanisms. Typically, due to the initial formation of the oil reservoir, there is a thin film of water separating the oil from the clay surface of a reservoir rock (Buckley 1996; Hirasaki 1991; Kovscek et al. 1993). As oil and clay surfaces are charged in the presence of brine, oil is attracted to the clay surface of the reservoir rock across this wetting layer. The mechanism proposals we wish to model suggest that the attraction between these surfaces reduces during LSW, which expands the water film and enables the release of oil.

In Sect. 2 we derive expressions for the surface charges of the oil and clay surfaces in a sandstone reservoir, assuming that each surface contains a number of charged exchange sites at which the reactions for each mechanism are able to take place. In Sect. 3, we determine the thickness of the film of water separating a static oil from a clay surface as a function of the concentration of the surrounding brine. This is done by considering a balance between the intermolecular forces (using the expressions for the surface charges derived in Sect. 2) and the capillary pressure, assuming that the oil and clay regions bounding the water film are large enough, relative to the film thickness, that they can be treated as semi-infinite domains. This approach is often used when considering the force acting between two charged plates (Ben-Yaakov and Andelman 2010; McCormack et al. 1995; Ohshima 1974a, b; Parsegian and Gingell 1972). In Sect. 4, we study how the molecular-scale mechanisms can affect the pore-scale movement of oil, by considering the motion of an oil slug moving through a water-filled clay pore. The film of water separating the oil from the clay surface acts as a 'slip layer', where the slip length is determined by the thickness of the film. Finally, in Sect. 5, we draw together our findings and compare the theoretical results with experimental observations.

## 2 Surface Reactions

When an oil droplet is suspended in water, polar compounds in the oil orientate themselves towards the surface due to the polarity of the surrounding $H_2O$ molecules; this generates a surface charge along the oil–water interface. The surface of clay minerals within the reservoir rock is also charged (Buckley 1996; Eslinger and Pevear 1988). One of the factors that is

important in the oil recovery process is the magnitude of the attraction between the oil and clay surface resulting from these surface charges, as this affects how easily oil is removed from the pore surface. This attraction can also influence other important reservoir properties, such as the contact angle formed at the oil–water–clay junction, which affects the wettability of the reservoir.

We wish to determine the charges of the oil and clay, assuming that the reactions in the MIE and pH mechanisms occur on the surface. Buckley (1996) considers a similar problem and determines the surface charge of the clay as a function of the pH of the surrounding brine, using a dissociation model at the exchange sites. We use a similar approach to derive expressions for the surface charges at the oil and clay surfaces, using a dissociation model for the reactions. In general, the mineralogy of the rock surface in an oil reservoir is heterogeneous. Clay minerals may only coat part of the surface, and, even within the clay, the exchange sites may by distributed unevenly. This results in a surface charge which varies along the surface of the reservoir rock. However, for simplicity, we treat the pore surface as homogenous throughout this paper.

### 2.1 Multicomponent Ionic Exchange

When a charged surface is submerged in a solution of ions, counterions are attracted to the surface and form a diffuse layer (Masliyah and Bhattacharjee 2006). The combination of the charged surface and oppositely charged diffuse layer is known as the 'electrical double layer'. As the concentration of ions in the bulk decreases, the thickness of this layer increases as a result of diffusion, and therefore, the thickness of the double layer increases; this is often referred to as 'electrical double layer expansion'.

In the multicomponent ionic exchange (MIE) mechanism, proposed by Lager et al. (2008), the thickness of the thin film of water separating the oil in a pore space from the clay surface increases in the low-salinity regime due to the expansion of the overlapping electrical double layers formed at the charged oil–water and clay–water interfaces. This encourages divalent cations, which form a bridge across the water layer and bind the negatively charged carboxylate ions on the oil surface to the negatively charged exchange sites on the clay surface, to be released and migrate into the bulk water regions, where the concentration of these ions is lower (due to the low-salinity injection). Monovalent cations replace the divalent cations at the negatively charged sites on the oil and clay surfaces, reducing the attraction of the oil to the clay surface, thus allowing the release of oil.

We suppose that the monovalent and divalent cations are sodium and calcium, $Na^+$ and $Ca^{2+}$, respectively, in our model. Whilst there may be competitive adsorption between ions of the same valency (e.g. $Mg^{2+}$ vs $Ca^{2+}$), we neglect this from our model since we are primarily interested in the competition between the monovalent and divalent ions. We model the reactions on the oil and clay surfaces separately, assuming that the bond formed by ligand bridging between the oil and clay surfaces can be modelled by the attraction between the surfaces resulting from the surface charges. We make this modelling choice in order to reduce the three-particle interaction of the $RCOO^- - Ca^{2+} - Clay^-$ bond to two separate two-particle interactions. This simplifies the modelling of the electric potential in the wetting film by allowing us to make the mean-field approximation. In Fig. 1a, we show the full three-particle mechanism, and in Fig. 1b, we show a schematic diagram of the reactions we model on each surface.

We assume that the clay surface contains a number of negatively charged exchange sites, $\chi^-$, which can either be unoccupied and negatively charged, occupied by a monovalent cation

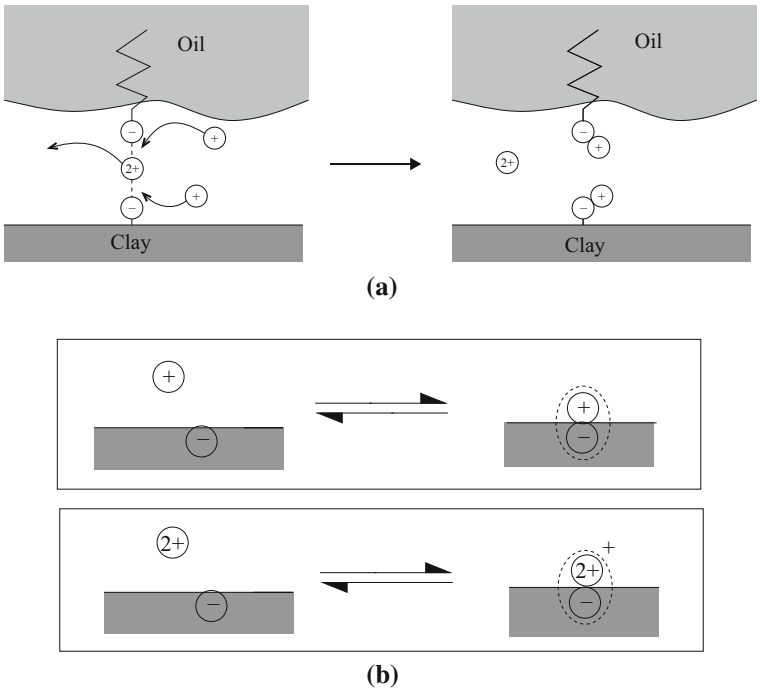


**Fig. 1** **a** Schematic diagram of the MIE mechanism as described by Lager et al. (2008), reproduced with permission from Wilmott et al. (2018b). **b** Diagram of the proposed model for the reactions occurring on each surface. The first reaction represents the adsorption of a monovalent cation to create a neutral site, and the second reaction represents the adsorption of a divalent cation to create a positively charged site

to form a neutral site, or occupied by a divalent cation to form a positively charged site. We suppose that the following reactions occur at the clay surface,

$$\chi^- + \mathrm{Na}^+ \rightleftharpoons \chi\mathrm{Na}, \qquad \chi^- + \mathrm{Ca}^{2+} \rightleftharpoons \chi\mathrm{Ca}^+. \tag{1}$$

By using the principle of mass action, and assuming that the reaction rates at the surface are fast enough (in comparison with typical flow rates within a reservoir) such that transient effects can be neglected, we obtain the following adsorption isotherm expressions on the capillary surface,

$$s_c = \frac{K_c^{(1)} c_c^{\mathrm{Na}^+} s_c^*}{1 + K_c^{(1)} c_c^{\mathrm{Na}^+} + K_c^{(2)} c_c^{\mathrm{Ca}^{2+}}}, \qquad s_c^+ = \frac{K_c^{(2)} c_c^{\mathrm{Ca}^{2+}} s_c^*}{1 + K_c^{(1)} c_c^{\mathrm{Na}^+} + K_c^{(2)} c_c^{\mathrm{Ca}^{2+}}}, \tag{2}$$

where $c_c^{\mathrm{Na}^+}$ and $c_c^{\mathrm{Ca}^{2+}}$ are the concentrations of monovalent $\mathrm{Na}^+$ ions and divalent $\mathrm{Ca}^{2+}$ ions, respectively, evaluated on the capillary surface, $s_c^*$ is the saturation concentration of exchange sites at the clay surface, $s_c$ is the surface concentration of sites occupied by monovalent ions, $s_c^+$ is the surface concentration of sites occupied by divalent ions, $K_c^{(1)} = [\chi\mathrm{Na}]/[\chi^-][\mathrm{Na}^+]$ is the equilibrium constant for sodium ions at the clay surface exchange sites, and $K_c^{(2)} = [\chi\mathrm{Ca}^+]/[\chi^-][\mathrm{Ca}^{2+}]$ is the equilibrium constant for calcium ions at the clay surface exchange sites. We have used the subscript $c$ to denote 'clay'.

Since the surface concentration of (negatively charged) unoccupied states is $s_c^- = s_c^* - s_c - s_c^+$, the surface charge density is given by $\sigma_c = q(s_c^+ - s_c^-) = q(2s_c^+ + s_c - s_c^*)$, where $q = 1.6 \times 10^{-19}$C is the charge of an electron. Using the expressions in (2), this reads

$$\sigma_c = q s_c^* \frac{K_c^{(2)} c_c^{\mathrm{Ca}^{2+}} - 1}{1 + K_c^{(1)} c_c^{\mathrm{Na}^+} + K_c^{(2)} c_c^{\mathrm{Ca}^{2+}}}. \tag{3}$$

We assume that similar reactions occur on the oil surface, due to the presence of carboxylic groups, and thus, the oil surface charge density is given by

$$\sigma_o = q s_o^* \frac{K_o^{(2)} c_o^{\mathrm{Ca}^{2+}} - 1}{1 + K_o^{(1)} c_o^{\mathrm{Na}^+} + K_o^{(2)} c_o^{\mathrm{Ca}^{2+}}}, \tag{4}$$

where the subscript $o$ denotes 'oil', and the variables have the obvious meanings. Using the values for the equilibrium constants found by Fletcher and Sposito (1989) and Liu et al. (2013) for a sample of montmorillonite, we find that $K_c^{(1)} \approx 8 \times 10^3 \mathrm{m}^3\,\mathrm{mol}^{-1}$ and $K_c^{(2)} \approx 9.7 \times 10^3\ \mathrm{m}^3\,\mathrm{mol}^{-1}$. The dissociation constants for the reactions on the oil surface are taken to be $K_o^{(1)} \approx 6 \times 10^{-4}\mathrm{m}^3\,\mathrm{mol}^{-1}$, since the p$K_a$ value for sodium acetate is approximately $-0.2$ (Fournier et al. 1998), and $K_o^{(2)} \approx 3 \times 10^{-4}\mathrm{m}^3\,\mathrm{mol}^{-1}$, since the p$K_a$ value for calcium acetate is approximately $-0.53$ (Joseph 1946). Using the values for the surface area and cation exchange capacity obtained for a sample of montmorillonite by Hang and Brindley (1970), we estimate that $s_c^* \approx 1.7 \times 10^{-8}\ \mathrm{mol\,m}^{-2}$. Lewis (1937) estimates the maximum charge at an oil–water interface to be $\sigma_o^{\max} \approx 0.12\ \mathrm{C\,m}^{-2}$. Hence, by using $\sigma_o^{\max} = q s_o^*$, we find that the saturation concentration is approximately $s_o^* \approx 1.2 \times 10^{-6}\ \mathrm{mol\,m}^{-2}$.

In order to evaluate the surface charge densities, we need to determine $c_c^{\mathrm{Na}^+}$, $c_c^{\mathrm{Ca}^{2+}}$, $c_o^{\mathrm{Na}^+}$, and $c_o^{\mathrm{Ca}^{2+}}$ as functions of the given bulk concentrations. In equilibrium, the ion concentrations satisfy the Boltzmann distribution (Andelman 1995; Masliyah and Bhattacharjee 2006),

$$c^i = c_*^i e^{-\frac{z_i q \phi}{k_B T}}, \tag{5}$$

where $\phi$ is the electric potential, $c^i$ is the concentration of ion $i$, $c_*^i$ is a function of the bulk concentration to be determined for each ion, $z_i$ is the valence of ion $i$ in the salt solution, $k_B \approx 1.4 \times 10^{-23}\mathrm{J\,K}^{-1}$ is Boltzmann's constant, and $T$ is the temperature, which we take to be 375 K as this is the temperature used during core-scale experiments by Lager et al. (2008).

We assume that the electric potential is small enough for us to make the Debye–Hückel approximation, $\phi \ll k_B T/q$ (Wilmott et al. 2018b). From (5), we find that the ion concentrations are uniform throughout the water phase, $c^i \sim c_*^i$. Hence, $c_*^i$ is equal to the bulk concentration of ion $i$, and $c_c^{\mathrm{Na}^+} = c_o^{\mathrm{Na}^+} = c_*^{\mathrm{Na}^+}$, $c_c^{\mathrm{Ca}^{2+}} = c_o^{\mathrm{Ca}^{2+}} = c_*^{\mathrm{Ca}^{2+}}$.

Hadia et al. (2012) performed core flood experiments with monovalent and divalent cation concentrations given by $c_{\mathrm{low}}^{\mathrm{Na}^+} \approx 15\ \mathrm{mol\,m}^{-3}$ and $c_{\mathrm{low}}^{\mathrm{Ca}^{2+}} \approx 0\ \mathrm{mol\,m}^{-3}$, respectively, in the low-salinity regime, and $c_{\mathrm{high}}^{\mathrm{Na}^+} \approx 600\ \mathrm{mol\,m}^{-3}$ and $c_{\mathrm{high}}^{\mathrm{Ca}^{2+}} \approx 140\ \mathrm{mol\,m}^{-3}$, respectively, in the high-salinity regime. A full list of parameter values used in this paper is given in Table 1.

In order to plot the effect of varying the concentrations of multiple ion species continuously from the low-salinity regime to the high-salinity regime, we introduce a parameter, $\tau$, such that $c_*^i(\tau) = c_{\mathrm{low}}^i + 10^\tau \left(c_{\mathrm{high}}^i - c_{\mathrm{low}}^i\right)$, where $c_{\mathrm{low}}^i$ is the concentration of ion $i$ in the low-salinity regime, and $c_{\mathrm{high}}^i$ is the concentration of ion $i$ in the high-salinity regime. For $\tau = 0$, we recover the high-salinity regime, and as $\tau \to -\infty$ we recover the low-salinity regime, which we approximate by $\tau = -6$ in the numerical simulations.

**Table 1** Parameter values

| Parameter | Value | Reference/notes |
|---|---|---|
| $c_{\text{low}}^{\text{Na}^+}$ | $15\ \text{mol m}^{-3}$ | Austad et al. (2010) |
| $c_{\text{high}}^{\text{Na}^+}$ | $600\ \text{mol m}^{-3}$ | Austad et al. (2010) |
| $c_{\text{low}}^{\text{Ca}^{2+}}$ | $0\ \text{mol m}^{-3}$ | Austad et al. (2010) |
| $c_{\text{high}}^{\text{Ca}^{2+}}$ | $140\ \text{mol m}^{-3}$ | Austad et al. (2010) |
| $c_*^{\text{H}_3\text{O}^+}$ | $10^{-2}\ \text{mol m}^{-3}$ | |
| $c_{\text{total}}^{\text{H}_3\text{O}^+}$ | $0.867\ \text{mol m}^{-3}$ | |
| $R$ | $1\ \bar{}\text{m}$ | Nelson (2009) |
| $L$ | $10\ \bar{}\text{m}$ | Nelson (2009) |
| $A_c$, $A_o$ | $2\pi\, 10^{-11}\text{m}^2$ | $2\pi RL$ |
| $V_w$ | $\pi\, 10^{-17}\text{m}^3$ | $\pi R^2 L$ |
| $\lambda$ | $1.5 - 0.2$ nm | $\lambda = \left(\frac{\varepsilon_w k_B T}{2\left(c_\infty^1 + 4c_\infty^2\right)q^2}\right)^{-\frac{1}{2}}$ |
| $\gamma$ | $0.02\ \text{J m}^{-2}$ | Buckley (1996) |
| $\mu_o$ | $0.01\ \text{kg m}^{-1}\ \text{s}^{-1}$ | Buckley (1996) |
| $\mu_w$ | $8.9 \times 10^{-4}\ \text{kg m}^{-1}\ \text{s}^{-1}$ | Buckley (1996) |
| $P$ | $0.045\ \text{N m}^{-2}$ | Wilmott et al. (2018b) |
| $T$ | $375°\text{K}$ | Lager et al. (2008) |
| $s_c^*$ | $1.7 \times 10^{-8}\ \text{mol m}^{-2}$ | Hang and Brindley (1970) |
| $s_o^*$ | $1.2 \times 10^{-6}\ \text{mol m}^{-2}$ | Lewis (1937) |
| $s_A^*$ | $1.2 \times 10^{-6}\ \text{mol m}^{-2}$ | Lewis (1937) |
| $s_B^*$ | $\approx 0\ \text{mol m}^{-2}$ | |
| $K_c^{(1)}$ | $8 \times 10^3\ \text{m}^3\ \text{mol}^{-1}$ | Fletcher and Sposito (1989) |
| $K_c^{(2)}$ | $9.7 \times 10^3\ \text{m}^3\ \text{mol}^{-1}$ | Fletcher and Sposito (1989) |
| $K_c^{(3)}$ | $10^{-4}\ \text{mol m}^{-3}$ | Liu et al. (2013) |
| $K_o^{(1)}$ | $6 \times 10^{-4}\ \text{m}^3\ \text{mol}^{-1}$ | Fournier et al. (1998) |
| $K_o^{(2)}$ | $3 \times 10^{-4}\ \text{m}^3\ \text{mol}^{-1}$ | Joseph (1946) |
| $K_o^{(A)}$ | $1.8 \times 10^{-2}\ \text{mol m}^{-3}$ | Kawaguchi et al. (1995) and Kütt et al. (2006) |
| $K_o^{(B)}$ | $10^{-7}\ \text{mol m}^{-3}$ | Tehan et al. (2002) |
| $\varepsilon_w$ | $5 \times 10^{-10}\ \text{C}^2\text{J}^{-1}\ \text{m}^{-1}$ | Malmberg and Maryott (1956) |
| $A$ | $10^{-20}$ J | Drummond and Israelachvili (2004) and Hirasaki (1991) |
| $q$ | $1.6 \times 10^{-19}$ C | |
| $k_B$ | $1.4 \times 10^{-23}\ \text{J K}^{-1}$ | |

In Fig. 2, we plot $\sigma_c$ and $\sigma_o$ against the salinity of the brine. We observe that the surface charge of both surfaces reduces as the salinity of the surrounding brine is reduced. The oil surface becomes more negatively charged in the low-salinity regime, and the clay surface goes from being positively charged to neutral as the salinity is reduced. Hence, the electrostatic

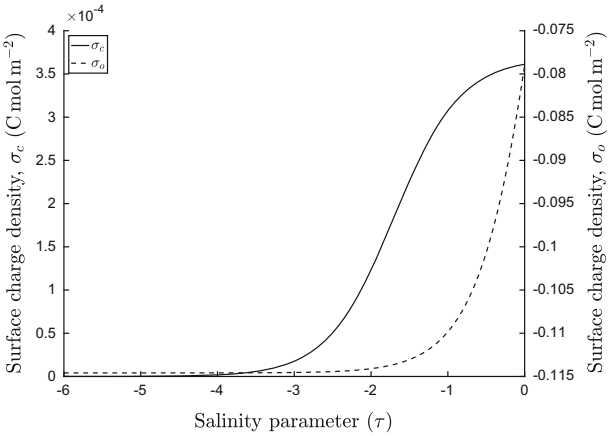


**Fig. 2** Surface charge densities of the clay and oil surfaces, given by (3) and (4), respectively, as functions of the salinity of the surrounding brine for the MIE mechanism, where $\tau = -6$ is the low-salinity regime, and $\tau = 0$ is the high-salinity regime. The solid line represents the surface charge of the clay surface, and the dashed line represents the surface charge of the oil surface

attraction between the surfaces decreases during a low-salinity waterflood, which is consistent with the theory that MIE enables the release of oil from clay surfaces. We will use the expressions for $\sigma_c$ and $\sigma_o$ to compute the total attraction between the two surfaces, combining electrostatic and screening effects, in Sect. 3.

### 2.2 Local pH Increase Mechanism

An alternative mechanism to explain the LSE, pH increase, was first proposed by Austad et al. (2010). In this mechanism, since the salinity of the surrounding brine decreases during LSW, the equilibrium at the surface of the clay is disturbed, resulting in a net desorption of cations, $Ca^{2+}$ in particular. As the number of vacant exchange sites on the clay surface increases due to this net desorption of cations, $H^+$ ions from the water adsorb onto the clay surface. This increases the pH locally in the wetting film between the oil and the clay, which enables the release of acidic and basic compounds which are adsorbed to the clay surface. In Fig. 3a, we show a schematic diagram of the acidic release mechanism, and in Fig. 3b, we present a schematic diagram of the basic release mechanism. In order to simplify these mechanisms so that we can use a dissociation model, we assume that the reactions occurring on the oil and clay surfaces are separate, as in the MIE case, with the oil–clay bond being the result of a net attraction between the surfaces. We suppose that the concentration of hydroxonium ions (i.e. the pH) in the bulk is given, independently of the salinity, but may vary locally in the thin water film. We thus assume that the reactions at the clay surface are given by

$$\chi^- + Ca^{2+} \rightleftharpoons \chi Ca^+, \qquad \chi H + H_2O \rightleftharpoons \chi^- + H_3O^+, \tag{6}$$

and the reactions on the oil surface are

$$RCOOH + H_2O \rightleftharpoons RCOO^- + H_3O^+, \qquad NHR_3^+ + H_2O \rightleftharpoons NR_3 + H_3O^+. \tag{7}$$

By following the same law-of-mass-action approach as for the MIE mechanism, and assuming that the concentration of water is constant, the adsorption isotherm expressions at the clay surface are given by

$$s_c = \frac{s_c^* c_c^{H_3O^+}}{c_c^{H_3O^+} + K_c^{(3)}\left(1 + K_c^{(2)} c_c^{Ca^{2+}}\right)}, \qquad s_c^+ = \frac{s_c^* K_c^{(2)} K_c^{(3)} c_c^{Ca^{2+}}}{c_c^{H_3O^+} + K_c^{(3)}\left(1 + K_c^{(2)} c_c^{Ca^{2+}}\right)}, \tag{8}$$

where $c_c^{H_3O^+}$ is the concentration of hydroxonium ions in the water film, evaluated at the surface of the clay, and $K_c^{(3)} = [\chi^-][H_3O^+]/[\chi H]$ is the equilibrium constant for the hydrogen ion exchange on the clay surface, which we take to be $K_c^{(3)} \approx 10^{-4}\,\mathrm{mol\,m^{-3}}$ since $pK_a \approx 7$ for the silicone complexes in montmorillonite (Liu et al. 2013). On the oil surface, the isotherm expressions are

$$s_A^- = \frac{s_A^* K_o^{(A)}}{c_o^{H_3O^+} + K_o^{(A)}}, \qquad s_B^+ = \frac{s_B^* c_o^{H_3O^+}}{c_o^{H_3O^+} + K_o^{(B)}}, \tag{9}$$

where $s_A^*$ is the surface saturation concentration of carboxylic acid molecules, $s_A^-$ is the surface concentration of deprotonated carboxylic acid groups, $s_B^*$ is the surface saturation concentration of polar aromatic compounds, $s_B^+$ is the surface concentration of protonated aromatic compounds, $K_o^{(A)} = [RCOO^-][H_3O^+]/[RCOOH]$ is the equilibrium constant for the acidic reaction, and $K_o^{(B)} = [NR_3][H_3O^+]/[NHR_3^+]$ is the equilibrium constant for the reaction involving the aromatic compound, in which $NR_3$ acts as a base. The subscripts $A$ and $B$ denote 'acidic' and 'basic', respectively. The $pK_a$ value for acetic acid is approximately 4.75 (Kawaguchi et al. 1995; Kütt et al. 2006), so we take $K_o^{(A)} \approx 1.8 \times 10^{-2}\mathrm{mol\,m^{-3}}$, and the $pK_a$ value for an amine group is approximately 10, with some variation depending on the compound (Tehan et al. 2002), so we take $K_o^{(B)} \approx 10^{-7}\mathrm{mol\,m^{-3}}$. The surface charge densities of the clay and oil surfaces are given by $\sigma_c = q(2s_c^+ + s_c - s_c^*)$ and $\sigma_o = q(s_B^+ - s_A^-)$, respectively. By substituting in equations (8) and (9), we find that

$$\sigma_c = q\frac{s_c^* K_c^{(3)}\left(K_c^{(2)} c_c^{Ca^{2+}} - 1\right)}{c_c^{H_3O^+} + K_c^{(3)}\left(1 + K_c^{(2)} c_c^{Ca^{2+}}\right)}, \tag{10}$$

$$\sigma_o = q\left(\frac{s_B^* c_o^{H_3O^+}}{c_o^{H_3O^+} + K_o^{(B)}} - \frac{s_A^* K_o^{(A)}}{c_o^{H_3O^+} + K_o^{(A)}}\right), \tag{11}$$

The concentration of $H_3O^+$ ions ranges from $10^{-5}$ – 1 $\mathrm{mol\,m^{-3}}$ for a solution with pH ranging from 3 to 8. Hence, for pH values typically observed in a reservoir, $K_o^{(B)} \ll c^{H_3O^+}$. We take the bulk pH to be 5 for the remainder of this paper, which corresponds to the concentration of hydroxonium ions being $10^{-2}$ $\mathrm{mol\,m^{-3}}$. Hadia et al. (2012) indicate that a high total acid number-to-total base number ratio is preferable for a low-salinity flooding, which corresponds to $s_B^* \ll s_A^*$. Hence, for simplicity, we will assume that $s_B^* \approx 0$ and $s_A^* = s_o^*$. Neglecting small terms, Eq. (11) reads

$$\sigma_o = -q\frac{s_A^* K_o^{(A)}}{c_o^{H_3O^+} + K_o^{(A)}}. \tag{12}$$

With the numerical values given, and neglecting small terms, we find that $\sigma_o$ is independent of $c_o^{Ca^{2+}}$ and depends only on $c_o^{H_3O^+}$ (i.e. the pH), as seen in (12).

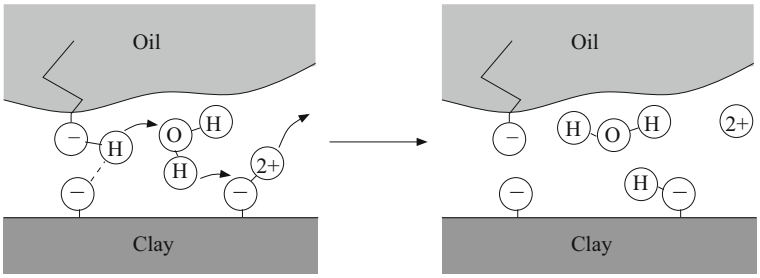


**(a)** Acidic reaction

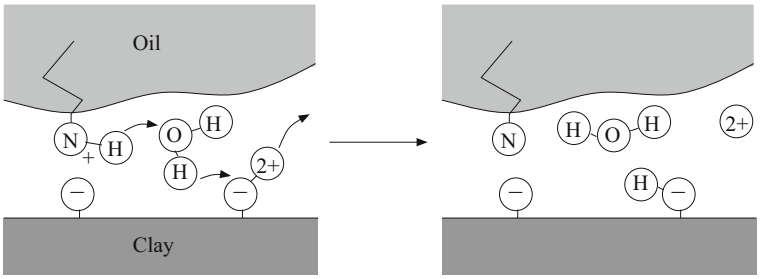


**(b)** Basic reaction

**Fig. 3** Diagram of the pH increase mechanism as described by Austad et al. (2010), for the **a** acidic (negatively charged), and **b** basic (positively charged) compounds on the oil surface

Similarly to the cation concentrations in the MIE mechanism, the concentration of hydroxonium ions satisfies $c^{H_3O^+} \sim c_*^{H_3O^+}$, where $c_*^{H_3O^+}$ is the bulk concentration of hydroxonium ions. Therefore, the local pH in the water film is spatially constant (so that $c_c^{H_3O^+} = c_o^{H_3O^+} = c^{H_3O^+}$) and equal to the pH specified in the bulk water surrounding the oil slug. Consequently, the reactions proposed by Austad et al. (2010) are not sufficient to explain a local increase in the pH of the brine using an ion dissociation model with the values for the parameters that we have used. This is a direct result of the fact that the surface charge densities of the oil and clay surfaces are not large enough to induce a noticeable variation in the ion concentrations within the water layer for the values used in this paper. Some types of clays and oils may have greater surface exchange site densities, $s_c^*$ and $s_o^*$, respectively, and may therefore react as suggested by Austad et al. This could explain why an increase in the pH is observed in some experiments, (Austad et al. 2010; Hadia et al. 2012), but not others (Lager et al. 2008; RezaeiDoust et al. 2011), despite there consistently being an increase in the amount of oil recovered.

Despite the pH being independent of the salinity, the surface charge density of the clay, $\sigma_c$, *does* vary with the concentration of $Ca^{2+}$. In Fig. 4, we plot $\sigma_c$ and $\sigma_o$ against $\tau$, for $-6 < \tau < 0$. The pH in the bulk is kept constant for all salinities, with $c^{H_3O^+} = 10^{-2}$ mol m$^{-3}$. As the salinity decreases, $\sigma_c$ decreases by a small amount, and $\sigma_o$ remains constant. This results in a small reduction in the electrostatic attraction between the two surfaces as the salinity of the surrounding brine is reduced. This is due to calcium desorbing from the clay surface, in exactly the same way as in the MIE mechanism [Eqs. (1b) and (6a) are identical].

The theory suggests that if the pH *does* increase during a core flood experiment, it would enhance the LSE. This can be seen by observing that $\sigma_o$ decreases with an increase in pH, in

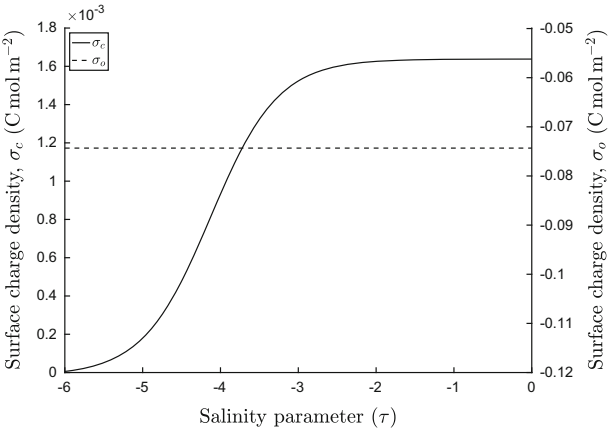


**Fig. 4** Surface charge densities of the clay and oil surfaces, given by (10) and (12), respectively, as functions of the salinity of the surrounding brine for the pH increase mechanism, where $\tau = -6$ is the low-salinity regime, and $\tau = 0$ is the high-salinity regime. The solid line represents the surface charge of the clay surface, and the dashed line represents the surface charge of the oil surface

Eq. (12). On the other hand, we expect that some experiments will display the LSE without a significant increase in pH, as it is not necessary in order for the surface charge of the clay to decrease. To study the contribution from each mechanism to the LSE for a particular clay sample, one could combine all of the reactions from both mechanisms into a single model, using exactly the same method as described here, and determine which terms dominate the expressions for a given set of parameters.

### 2.3 Global pH Increase

By specifying the bulk pH in Sect. 2.2, we restricted our attention to local variations in the pH in the thin wetting film. We briefly consider the extension to this model in which we specify the total number of $H_3O^+$ ions throughout a particular domain, and allow adsorption and desorption at the surface exchange sites to affect the concentration of hydroxonium ions in the bulk. We refer to this as the global pH increase model.

We define $V_w$ to be the total volume of water in the domain, and $A_c$ and $A_o$ to be the surface areas of the clay and oil, respectively. For simplicity, we choose $V_w = \pi \times 10^{-17}\ \mathrm{m}^3$ and $A_c = A_o = 2\pi \times 10^{-11}\ \mathrm{m}^2$ as these are the volume and surface area, respectively, of a cylindrical 'pore throat' with radius 1 μm and length 10 μm. As in Sect. 2.2, we define $c^{H_3O^+}$ to be the spatially constant concentration of hydroxonium ions.

By balancing the total number of ions in the domain with the number of ions in the bulk and the number of ions adsorbed to the surfaces, we find that

$$V_w c_{\mathrm{total}}^{H_3O^+} = V_w c^{H_3O^+} + A_c s_c + A_o(s_A + s_B^+), \tag{13}$$

where $V_w c_{\mathrm{total}}^{H_3O^+}$ is the total number of ions (so that $c_{\mathrm{total}}^{H_3O^+}$ would be the concentration if all of the ions were in the water). Substituting $s_c$, $s_A$ and $s_B^+$ [given by (8) and (9)], into (13),

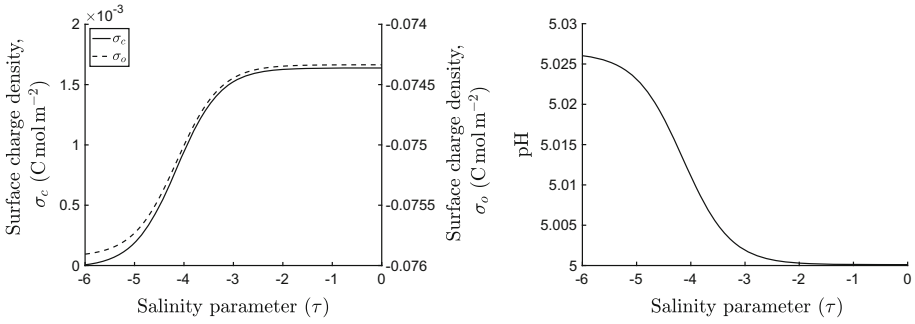


**Fig. 5** **a** Surface charge densities of the clay and oil surfaces, given by (10) and (12), respectively, as functions of the salinity of the surrounding brine for the global pH increase mechanism. The concentration of hydroxonium ions, $c^{H_3O^+}$ is determined from 14. **b** pH as a function of the salinity for the global increase mechanism. The parameter values used are given in Table 1

using the fact that $c^{H_3O^+} = c_c^{H_3O^+} = c_o^{H_3O^+}$, and assuming that $s_B^* = 0$, we write $c^{H_3O^+}$ implicitly in terms of $c_{\text{total}}^{H_3O^+}$ and $c_c^{Ca^{2+}}$ as

$$V_w c_{\text{total}}^{H_3O^+} = V_w c^{H_3O^+} + \frac{A_c s_c^* c^{H_3O^+}}{c^{H_3O^+} + K_c^{(3)}\left(1 + K_c^{(2)} c_c^{Ca^{2+}}\right)} + \frac{A_o s_A^* c^{H_3O^+}}{c^{H_3O^+} + K_o^{(A)}}. \tag{14}$$

For a given concentration of divalent ions (i.e. a given salinity), we solve (14) for $c^{H_3O^+}$ and substitute the result into (10) and (12) to determine the effective surface charge densities at the surfaces of the oil and the clay.

In Fig. 5a, we plot $\sigma_o$ and $\sigma_c$ against the salinity parameter, $\tau$, for $-6 < \tau < 0$. We select $c_{\text{total}}^{H_3O^+} = 0.867\,\text{mol}\,\text{m}^{-3}$ so that $c^{H_3O^+} = 0.01\,\text{mol}\,\text{m}^{-3}$ (i.e. pH=5) in the high-salinity regime. We observe that the surface charge densities of both surfaces decrease as the salinity decreases, which is consistent with experimental observations. In Fig. 5b, we plot the pH against $\tau$ and observe that there is a slight increase in the pH as the salinity decreases. Whilst this is qualitatively consistent with the pH increase mechanism, the quantitative increase in the pH is significantly smaller than observed experimentally by Austad et al. (2010). This is likely partly due to the simplistic model for the ion exchange reactions occurring at the oil and clay surfaces. However, it is worth noting that the pH increase is sensitive to the surface area of the clay, since the greater the surface area, the greater the number of sites at which hydrogen ions can be adsorbed and consequently removed from the surrounding fluid. The cylindrical pore throat model will significantly underestimate the surface area of the clay due to the typically irregular shape of reservoir rock, surface roughness, and the presence of asperities within the clay.

To illustrate this, in Fig. 6a we plot $\sigma_o$ and $\sigma_c$ against the salinity parameter, $\tau$, for the case $A_c = 2\pi \times 10^{-9}\,\text{m}^2$. We observe that, as the salinity decreases, the surface charge of the clay decreases by the same amount as in the $A_c = 2\pi \times 10^{-11}\,\text{m}^2$ case (Fig. 5a), but that the decrease in the oil surface charge is greater. In Fig. 6b, we plot the pH against $\tau$ and observe that the pH increases by approximately 2, which is consistent with the observations of Austad et al. (2010).

Hence, the surface area-to-volume ratio within the reservoir rock plays an important role for the global pH increase mechanism since the relatively low concentration of hydrogen

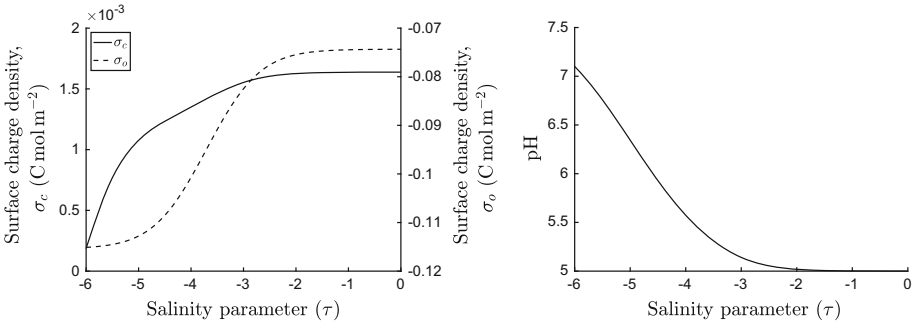


**Fig. 6** **a** Surface charge densities of the clay and oil surfaces, as functions of the salinity of the surrounding brine for the global pH increase mechanism. **b** pH as a function of the salinity for the global increase mechanism. The surface area of the clay is given by $A_c = 2\pi \times 10^{-9}\,\mathrm{m}^2$, and otherwise, the parameter values used are given in Table 1

ions within the brine may be significantly affected by adsorption and desorption at the clay surface. This is in contrast to the MIE mechanism, in which the relatively high concentration of $Na^+$ and $Ca^{2+}$ ions within the surrounding brine is unaffected by the small amount of adsorption and desorption at the surface. It may be possible to use this observation to distinguish between the two mechanisms experimentally. If global pH increase is the dominant low-salinity mechanism, then the pH of the surrounding fluid, and consequently the surface charge of the oil phase, depends on the surface area-to-volume ratio of the reservoir rock, whereas for the MIE mechanism this is not the case.

The global pH increase mechanism reduces to the local pH increase case in the limit in which the ratio of the number of exchange sites on the surface of the clay to the number of hydroxonium ions in the water phase is small, $s_c^* A_c / V_w c_{\mathrm{total}}^{\mathrm{H_3O^+}} \ll 1$. Hence, in this case, the additional algebraic complexity of the global increase model is unnecessary and the local model may be used. Otherwise, the full global model is required.

## 3 Film Thickness of Static Oil

Due to surface asperities and the varying mineralogy of the reservoir rock, the oil phase within a reservoir is only in effective contact with the solid surface in localised 'pinning regions' (Brady et al. 2015; Schmatz et al. 2015), as shown in Fig. 7a. Within these pinning regions, the oil phase adsorbs to the clay surface across a thin water layer according to the salinity-dependent ion exchange reactions described in Sect. 2. The thickness of this water film is determined by a balance between intermolecular forces (which consists of van der Waals, structural, and electrostatic forces), hydrodynamic forces (when the oil–water system is in motion), and capillary forces.

There are numerous theoretical studies (Hirasaki 1991; Kovscek et al. 1993; Wong et al. 1992) discussing the thickness and stability of thin films separated by charged surfaces based on the Derjaguin–Landau–Verwey–Overbeek (DLVO) theory of colloidal stability (Derjaguin and Landau 1941; Verwey and Overbeek 1948). Hirasaki (1991) studies the thickness of the film below a static oil droplet by balancing the disjoining pressure with the capillary pressure and concludes that, for a given capillary pressure, there are up to two locally stable thicknesses

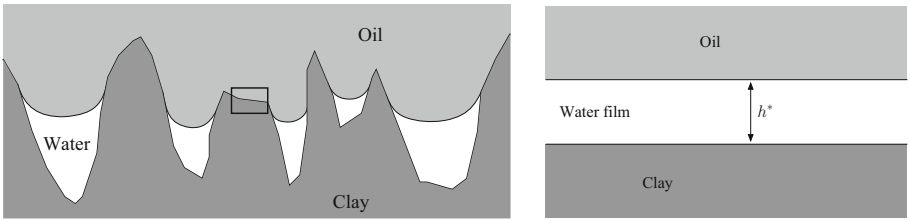


**Fig. 7** **a** Diagram of static oil in effective contact with a clay surface in a number of pinning regions. **b** Expanded view of the pinning region indicated in figure (**a**), showing that for a sufficiently thin film, the oil and clay surfaces can be treated as two planes

for the water layer. If the film is formed by an oil slug advancing into a water-filled pore, the film approaches the larger stable state. However, this thickness is only locally stable, and for a large enough disruption, this film can rupture and reduce to the thinner stable state. Kovscek et al. (1993) also conclude that there are two locally stable film thicknesses. They find that the thinner stable thickness exists due to structural forces preventing the layer from collapsing, and is only several molecules thick. Since we are primarily interested in the larger, salinity-dependent film thickness, we will neglect structural forces from our model. Wong et al. (1992) use a similar approach to determine the film thickness and the effective contact angle of oil in a capillary, and they conclude that the disjoining pressure isotherm must contain a 'spike' in order to observe a finite effective contact angle. Such a spike may be introduced by including the effect of van der Waals forces, which in turn affects the thickness of the wetting film. Hence, as well as studying the effect of the surface charges on the film thickness, we will include the effect of van der Waals forces in our model.

Since we are primarily interested in the effect of salinity on the oil–water–clay system, we focus our attention on the pinning regions in which the oil is separated from the clay by a thin water layer, as shown by the boxed region in Fig. 7a. We assume that the water film is thin enough relative to the size of the asperity such that we can treat the clay and oil surfaces as charged planes, located at $y = 0$ and $y = h^*$, respectively, as shown in Fig. 7b. The film thickness, $h^*$, is to be determined as part of the solution to our model.

We assume that there is a pressure difference across the oil–water interface given by the capillary pressure, $P_c$, which balances the disjoining pressure, $\Pi$, and from this balance we will determine the thickness of the wetting film, $h^*$. In transport equilibrium, the electric potential, $\phi$, is given by the Poisson–Boltzmann equation (Andelman 1995; Masliyah and Bhattacharjee 2006),

$$\frac{\mathrm{d}^2\phi}{\mathrm{d}y^2} = \begin{cases} 0 & y > h^*, \\ -\sum_i \frac{z_i q c^i}{\varepsilon_w}, & 0 < y < h^*, \\ 0, & y < 0, \end{cases} \tag{15}$$

$$c^i = c^i_* e^{-\frac{z_i q \phi}{k_B T}}, \tag{16}$$

where $\varepsilon_w \approx 5 \times 10^{-10}\mathrm{C}^2\mathrm{J}^{-1}\mathrm{m}^{-1}$ (Malmberg and Maryott 1956) is the permittivity of the water phase.

We assume that $\phi$ is bounded as $y \to \pm\infty$ so that, from (15), $\frac{\mathrm{d}\phi}{\mathrm{d}y} = 0$ for $y < 0$ and $y > h^*$. Hence, as the oil–water and clay–water interfaces are charged, $\phi$ satisfies

$$\left.\frac{\mathrm{d}\phi}{\mathrm{d}y}\right|_{y=0^+} = \frac{\sigma_c}{\varepsilon_w}, \qquad \left.\frac{\mathrm{d}\phi}{\mathrm{d}y}\right|_{y=h^{*-}} = -\frac{\sigma_o}{\varepsilon_w}. \tag{17}$$

We also assume that the brine is electrically neutral, $\sum_i z_i c_*^i = 0$, and that the charge on the surfaces is small enough for us to make the Debye–Hückel approximation, $\phi \ll k_\mathrm{B}T/q$. These assumptions enable us to make two simplifications. First, from (16) we find that the leading-order concentration is given by $c^i \sim c_*^i$, so that, to leading order, we can use the concentrations of the ions in the bulk in Eqs. (3), (4), (10), and (12) when calculating the surface charge on the oil and clay surfaces. Second, by substituting (16) into (15), expanding the exponential terms, and neglecting $O(\phi^2)$ terms and higher, we find that Eq. (15) simplifies to

$$\frac{\mathrm{d}^2\phi}{\mathrm{d}y^2} = \frac{1}{\lambda^2}\phi, \qquad \text{for } 0 < y < h^*, \tag{18}$$

where $\lambda = \left(\varepsilon_w k_B T/q^2 \sum_i z_i^2 c_*^i\right)^{1/2}$ is the Debye length. By integrating twice and applying the boundary conditions, (17), we find that in the water film,

$$\phi = \frac{\lambda}{\varepsilon_w \sinh\frac{h^*}{\lambda}}\left(\sigma_c \cosh\frac{h^*-y}{\lambda} + \sigma_o \cosh\frac{y}{\lambda}\right). \tag{19}$$

The expression for the electrostatic component of the disjoining pressure, $\Pi_\mathrm{el}$, acting between the surfaces is found by multiplying (15) by $\varepsilon_w \frac{\mathrm{d}\phi}{\mathrm{d}y}$ and integrating to obtain

$$\Pi_\mathrm{el} = k_\mathrm{B}T \sum_i c_*^i \left(e^{-\frac{z_i q\phi}{k_\mathrm{B}T}} - 1\right) - \frac{\varepsilon_w}{2}\left(\frac{\mathrm{d}\phi}{\mathrm{d}y}\right)^2. \tag{20}$$

We have selected the arbitrary constant resulting from the integration in order to write $\Pi_\mathrm{el}$ as the sum of the osmotic pressure and the electrostatic pressure resulting from the interaction between the two charged surfaces (Ben-Yaakov and Andelman 2010; McCormack et al. 1995; Xiao et al. 2013). Substituting (19) into (20), and neglecting $\mathcal{O}(q[\phi]/k_B T)$ terms and higher, the electrostatic component of the disjoining pressure is found to be

$$\Pi_\mathrm{el} \sim \frac{\sigma_c^2 + 2\sigma_c\sigma_o \cosh\frac{h^*}{\lambda} + \sigma_o^2}{2\varepsilon_w \sinh^2\frac{h^*}{\lambda}}. \tag{21}$$

Another contribution to the disjoining pressure is the pressure due to van der Waals forces, which, between two planar surfaces, is given by

$$\Pi_{\mathrm{v}dW} = -\frac{A}{6\pi h^{*3}}, \tag{22}$$

where $A$ is the Hamaker constant, which can be attractive or repulsive depending on the substances constituting the three phases either side and between the interfaces. For an oil–brine–clay system, we take the Hamaker constant to be $10^{-20}$J (Drummond and Israelachvili 2004; Hirasaki 1991). It is possible to include other terms in the disjoining pressure, such as the contribution from structural forces (Hirasaki 1991); however, we neglect these additional effects. The total disjoining pressure is given by the sum of the individual components; for our model, $\Pi = \Pi_\mathrm{el} + \Pi_{\mathrm{v}dW}$.

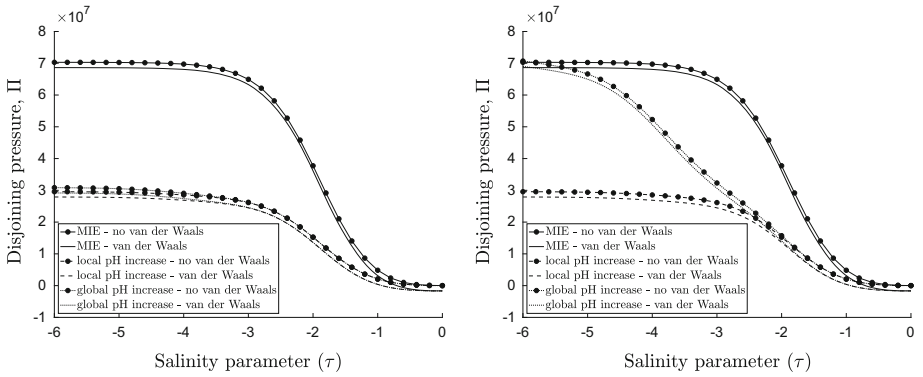


**Fig. 8** **a** Disjoining pressure, $\Pi$, versus salinity for the MIE, local pH increase, and global pH increase mechanisms, comparing the results with and without the inclusion of van der Waals forces. The film thickness is chosen to be $h^* = 1 \times 10^{-9}$m, and otherwise, the parameter values are given in Table 1. **b** Disjoining pressure, $\Pi$, versus salinity for the three mechanisms for the $A_c = 2\pi \times 10^{-9}\,\mathrm{m}^2$ case

In Fig. 8a, we plot the disjoining pressure, $\Pi$, against the salinity parameter, $\tau$ for the MIE, local pH increase, and global pH increase mechanisms, with and without the inclusion of the van der Waals term. The film thickness is chosen to be $h^* = 1 \times 10^{-9}$m. We observe that, for all three mechanisms, the disjoining pressure increases as the salinity decreases, resulting in greater repulsion between the oil and clay surfaces in the low-salinity regime, which may contribute to the LSE. We observe that the global pH increase model is in agreement with the local pH increase model due to the fact that $s_c^* A_c / c_{\mathrm{local}}^{\mathrm{H_3O^+}} V_w = 4 \times 10^{-2}$ is small, as discussed in Sect. 2.3. The van der Waals force is attractive for the parameter values used, acting to decrease the disjoining pressure by a constant value for a given film thickness.

In Fig. 8b, we plot $\Pi$ against $\tau$ for the three mechanisms for the case in which the surface area of the clay is given by $A_c = 2\pi \times 10^{-9}\,\mathrm{m}^2$. (And otherwise, the parameter values are the same as previously, given in Table 1.) We observe that the MIE and local pH increase mechanisms are unaffected by the change in the surface area of the clay (in comparison with Fig. 8a), but that the disjoining pressure is greater in the low-salinity regime for the global pH increase mechanism. By studying the effect of the surface area of the clay on the LSE, this result may be used to help distinguish between the MIE and global pH increase mechanisms experimentally.

The film thickness is found by assuming that the system is in equilibrium when the disjoining pressure is equal to the capillary pressure, $\Pi = P_c$. For oil trapped in a pore throat of radius 1¯m (Nelson 2009), with surface tension $\gamma = 0.02\,\mathrm{J\,m^{-2}}$ (Buckley 1996), the capillary pressure is given by $P_c = 2\gamma/R \approx 4 \times 10^6\,\mathrm{N\,m^{-2}}$. Using expressions (22) and (21), this results in the transcendental equation for the film thickness, $h^*$, given by

$$P_c = \frac{\sigma_c^2 + 2\sigma_c\sigma_o \cosh\frac{h^*}{\lambda} + \sigma_o^2}{2\varepsilon_w \sinh^2\frac{h^*}{\lambda}} - \frac{A}{6h^{*3}}. \tag{23}$$

Although it is not possible to rearrange this equation to write down an explicit expression for the film thickness, we can gain some insight into the effect of LSW on $h^*$ by neglecting the van der Waals term. With this term removed, the film thickness is given by

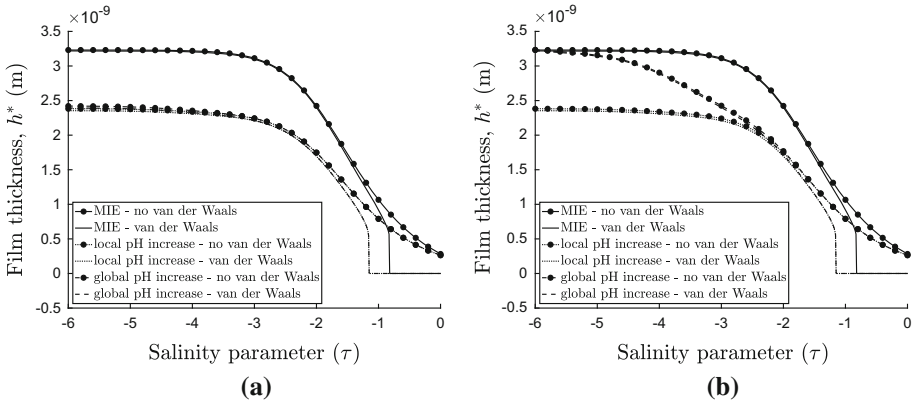


**Fig. 9** **a** Film thickness versus salinity for the MIE, local pH increase, and global pH increase mechanisms, with and without the inclusion of van der Waals forces, given by equations (23) and (24), respectively. The parameter values are given in Table 1. **b** Film thickness versus salinity for the three mechanisms for the $A_c = 2\pi \times 10^{-9}\,\mathrm{m}^2$ case

$$h^* = \lambda \cosh^{-1}\left[\frac{\sigma_o\sigma_c + \sqrt{\left(\sigma_c^2 + 2P_c\varepsilon_w\right)\left(\sigma_o^2 + 2P_c\varepsilon_w\right)}}{2P_c\varepsilon_w}\right]. \tag{24}$$

Note that $h^*$ increases linearly with the Debye length, which is inversely proportional to the square root of the ion concentrations, $\lambda \sim (\sum_i z_i^2 c_*^i)^{-1/2}$. As the salinity of the brine is reduced, $\lambda$ increases. This is referred to as electric double layer expansion and is often cited as one of the main factors contributing to the LSE (Ligthelm et al. 2009; Nasralla et al. 2013, 2014). However, the thickness of the film has a more complicated functional dependence on the ion concentrations, due to the overlapping fields of the charged surfaces, and consequently, the increase in film thickness is due to a combination of both the electric double layer expansion and the variation in the surface charges.

In Fig. 9a, we plot the film thickness, $h^*$, against the salinity parameter, $\tau$, for the three mechanisms, with and without the inclusion of the van der Waals term. We observe that, excluding van der Waals forces, the film thickness increases as the salinity decreases for all three mechanisms. We also observe that the MIE film thickness is always greater than the local and global pH increase film thicknesses. The magnitude of the film thickness is consistent with experimental data gathered by Lee et al. (2010), in which the film thickness was directly measured using small angle neutron scattering.

At low-salinities, the van der Waals term only results in a small correction to the solution. As the salinity increases, the film thickness decreases smoothly until a critical point at which the finite film thickness solution no longer exists. At this point, the attractive van der Waals component of the disjoining pressure dominates the electrostatic component ($\Pi_{\mathrm{vdW}} \propto 1/h^3$, whereas $\Pi_{\mathrm{el}} \propto 1/h^2$ for small $h$), resulting in the film thickness reducing to zero. However, structural forces due to the finite size of the ions need to be considered for films $\mathcal{O}(10^{-10}\,\mathrm{m})$ or less. Hence, in practice, the film thickness will not reduce to zero thickness as the salinity increases. Instead, a repulsive potential will dominate, causing the film to have a small, but finite, thickness. Hirasaki (1991) discusses the inclusion of structural forces in more depth.

In Fig. 9b, we plot the film thickness against the salinity for the three mechanisms for the $A_c = 2\pi \times 10^{-9}\,\mathrm{m}^2$ case. As expected, the film thickness for the global pH increase

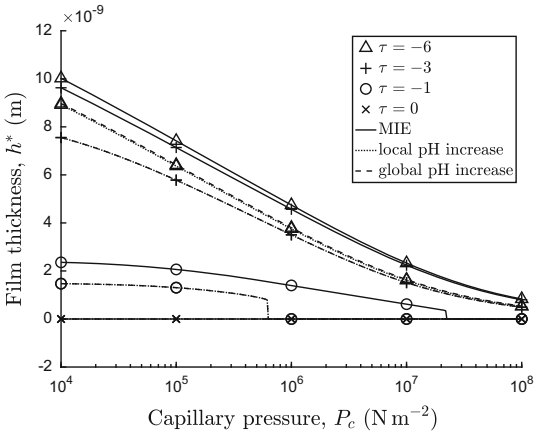


**Fig. 10** Film thickness versus capillary pressure for a range of salinities, for the MIE, local pH increase, and global pH increase mechanisms, given in Eqs. (23) and (24), respectively. The parameter values used are given in Table 1

mechanism depends on the surface area of the clay, but the film thicknesses for the other two mechanisms do not.

In Fig. 10, we plot the film thickness as a function of the capillary pressure, for salinities given by $\tau = -6, -3, -1, 0$, for the three mechanisms with the inclusion of van der Waals forces. We choose the range of capillary pressures to be $10^4\,\mathrm{N\,m^{-2}} < P_c < 10^8\,\mathrm{N\,m^{-2}}$, as this spans the range of pressures typically found in an oil reservoir. The film thickness increases as the capillary pressure decreases for all three mechanisms. At higher salinities, there is a critical capillary pressure at which the film thickness suddenly decreases to zero, since the attractive van der Waals forces dominate the electrostatic forces and the larger stable film thickness ceases to exist. Hirasaki (1991) discusses this critical point in more detail; however, in their model the film thickness reduces to a small, but nonzero, value due to the inclusion of structural forces.

One of the claims made by Austad et al. (2010) and Lager et al. (2008) is that the MIE and pH increase mechanisms allow the 'release' of oil during a low-salinity waterflood, indicating that when the salinity is reduced, the oil moves away from the solid surface. This requires a force acting on the oil–water interface in the direction away from the clay surface. However, for spherical oil droplets, or oil occupying a water-wet pore space, the capillary pressure is positive, which results in a force on the oil–water interface acting *towards* the clay surface.

To explain how an increase in the film thickness leads to a greater oil recovery, we propose an alternative pore-scale mechanism. If the viscosity of the oil is greater than the viscosity of the water, as is often the case in an oil reservoir, the wetting film acts as a 'slip layer', allowing the oil to slide along the clay surface. The magnitude of this slip is measured by the effective slip length, which is given by the thickness of the water film (Wilmott et al. 2018b). Hence, during a low-salinity waterflood, the film thickness increases and therefore the mobility of the oil phase increases. In terms of Buckley–Leverett theory on the core scale, this corresponds to an increase in the relative permeability of the oil phase, which results in a greater water saturation behind the shock front during a waterflood. Consequently, an increase in the film thickness on the pore scale results in a decrease in the residual oil on the macroscopic scale.

## 4 Moving Oil Slug

### 4.1 Film Thickness

To study the effect of the film thickness on the mobility of oil, we consider the steady motion of an oil slug of length $L_o$ through a brine-filled clay pore throat, subject to an applied pressure, $P$. On the pore scale, an increase in the mobility of the oil phase is realised as an increase in the velocity of the oil slug for a given applied pressure. Hence, in this section, our aim is to determine the velocity of the oil slug, which we will use as a proxy for the macroscopic oil mobility.

Experimental work by Brady et al. (2015) and Schmatz et al. (2015) indicates that an oil drop is in effective contact with the clay only over certain regions (pinning regions). Here, in order to make analytical progress, we simplify the complex geometry of a pore throat (recall Fig. 7a) by modelling it as a capillary tube of length $L$ and radius $R$, and suppose that the whole length of the drop is a pinning region, as shown in Fig. 11a. By studying the problem in a simplified geometry, we gain insight into the chemical and fluid dynamical processes which occur within the pore throat, without the mathematical complications introduced by complex geometries. The framework can be extended to more realistic configurations, including surface roughness (Raeesi et al. 2013), at the cost of algebraic complexity. There are also many techniques for computing slip flow through irregularly shaped channels (Bahrami et al. 2009; Ghosal 2002; Wilmott et al. 2018a) which may be useful for extending the model in this direction. Additional effects such as contact line pinning and the viscoelastic oil–brine interface must also be included in order to study the effect of oil trapping and pinning within the pore. However, we neglect these effects from our model in order to focus on the effect of the MIE and pH increase mechanisms on the movement of mobile oil.

We compare the MIE and pH increase mechanisms by assuming that the clay and oil surfaces are charged, with surface charge densities given by (3) and (4) for the MIE mechanism, and (10) and (12) for the pH increase mechanism. For a moving oil slug, hydrodynamic forces due to the receding fluid being squeezed between the oil and clay surfaces as the oil slug advances contribute to the film thickness, in addition to the intermolecular and capillary forces, and (23), which gives the film thickness in the static case, no longer holds *a priori*. Hence, we must derive an expression for the film thickness using a dynamic model.

In Wilmott et al. (2018b), we consider the motion of an oil slug in the absence of van der Waals forces in the MIE case. To include the van der Waals term, we modify the stress balance boundary condition on the oil–water interface according to

$$p_o - p_w = \Pi + \frac{\gamma h_{xx}}{(1+h_x^2)^{3/2}}, \tag{25}$$

where $p_o$ and $p_w$ are the pressures on the oil side and water side of the interface, respectively, and $h$ is the (static) profile of the oil–water interface in a reference frame moving with the oil slug, as shown in Fig. 11b. This is commonly referred to as the augmented Laplace–Young equation (Hirasaki 1991; Kovscek et al. 1993; Wong et al. 1992).

By following the same methodology as in Wilmott et al. (2018b), but including the van der Waals term in the Laplace–Young boundary condition, we find that the film thickness, $h^*$, is given by the solution to the third-order o.d.e,

$$6V\frac{h-h^*}{h^3} = \gamma h_{xxx} + \left(\frac{\sigma_c^2 + 2\sigma_c\sigma_o\cosh\frac{h}{\lambda} + \sigma_o^2}{2\varepsilon_w \sinh^2\frac{h}{\lambda}} - \frac{A}{6h^3}\right)_x, \tag{26}$$

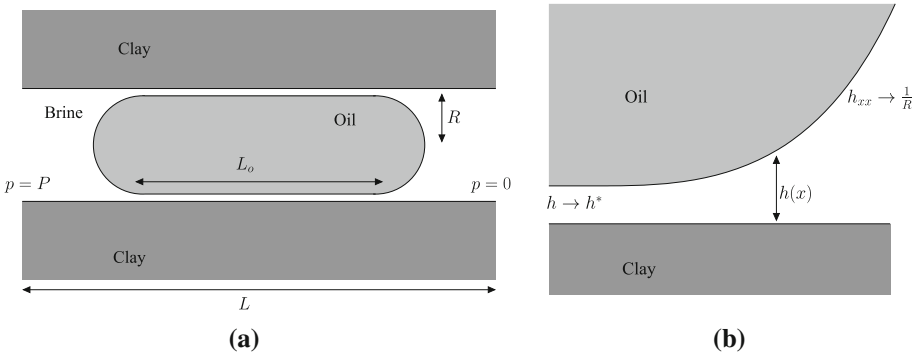


**Fig. 11** **a** Schematic diagram of an oil slug in a capillary, moving under the action of an applied pressure, $P$. The thickness of the water film below the oil slug has been exaggerated for illustrative purposes. **b** Expanded view of the region near the apparent contact point at the front of the oil slug. The profile of the oil–water interface is given by $h(x)$, and the limiting behaviour of $h$ in the direction of the thin film ($x \to -\infty$) and the direction of the meniscus ($x \to \infty$) is indicated on the diagram

subject to $h \to h^*$ as $x \to -\infty$, and $h_{xx} \to 1/R$ as $x \to \infty$. The velocity of the oil slug, $V$, is found to satisfy

$$V = \frac{R^2 P}{\mu_w L\left[1 + \left(\frac{\mu_o}{\mu_w} - 1\right)\frac{L_o}{L}\right]}\left\{\frac{1}{3} + \frac{\mu_o L_o\left(\frac{\mu_o}{\mu_w} - 1\right)}{\mu_w L R\left[1 + \left(\frac{\mu_o}{\mu_w} - 1\right)\frac{L_o}{L}\right]}h^* + \frac{\gamma}{3PL^2}(r^- - r^+)\right\}, \tag{27}$$

where $r^{\pm}$ are the radii of curvature of the front (+) and rear (−) menisci of the oil slug. Following the methodology of Wilmott et al. (2018b), these terms are given by

$$r^{\pm} = \lim_{x \to \pm\infty} R - h + \frac{L^2}{2R}h_x^2. \tag{28}$$

Throughout this paper, the relationship between the salinity and the fluid dynamics is expressed in terms of the film thickness. However, the film profile can be related to the effective equilibrium contact angle by integrating the expression for the disjoining pressure, $\Pi(h)$, from $h = h^*$ to $h \to \infty$ (Hirasaki 1991; Kovscek et al. 1993; Wong et al. 1992). Whilst this integration is straightforward, it only enables us to compute the static contact angle in the limit $V \to 0$. To determine the moving contact angles at the front and rear of the oil slug, we substitute the expressions for $r^{\pm}$ given by (28) into the geometrical relationship between the menisci radii and the effective contact angles, $\cos\theta^{\pm} = R/r^{\pm}$. Hence, a change in the film thickness is related to a wettability alteration, which is often cited as the cause of the LSE (Bartels et al. 2017; Mahani et al. 2015).

To determine the film thickness, we must solve (26) and (27) simultaneously. However, provided that $P$, and therefore $V$, is sufficiently small, i.e. the oil slug is moving slowly, we can simplify the problem. In the limit $P \to 0$, we find that, by following the methodology of Wilmott et al. (2018b), the film thickness, $h^*$, is given by (23). This is to be expected, since in the slow-moving limit we expect to recover the static solution. This is often the case for typical flow rates observed in a reservoir, where typically the pressure drop along the length of the pore is $P \approx 0.045\,\mathrm{N\,m^{-2}}$ (Wilmott et al. 2018b). However, this may vary significantly depending on the particular reservoir conditions being studied.

### 4.2 Velocity for Small $P$

By following the same methodology as Wilmott et al. (2018b), we find that, for small $P$, the speed of the oil slug is given by

$$V \approx \frac{R^2 P}{\mu_w L} \frac{\left\{ \frac{1+\left(\frac{\mu_o}{\mu_w}-1\right)\frac{L_o}{L}}{3} + \frac{\mu_o L_o \left(\frac{\mu_o}{\mu_w}-1\right)}{\mu_w L R} h^* \right\}}{\left[1+\left(\frac{\mu_o}{\mu_w}-1\right)\frac{L_o}{L}\right]^2 + 2\frac{R}{L}\left[1+\left(\frac{\mu_o}{\mu_w}-1\right)\frac{L_o}{L}\right]\int_{-\infty}^{\infty} \frac{(h-h^*)^2}{h^3}\mathrm{d}x}, \tag{29}$$

where $h^*$ is given by (23), and the integral is evaluated using the solution to (26).

In Fig. 12a, we plot the speed of the oil slug, $V$, against the salinity parameter, $\tau$, for the MIE, local pH increase, and global pH increase mechanisms. We choose $\mu_o = 0.01\,\mathrm{kg\,m^{-1}s^{-1}}$ and $\mu_w = 8.9 \times 10^{-4}\,\mathrm{kg\,m^{-1}s^{-1}}$ as the viscosity of the oil and water, respectively (Buckley 1996). We choose the radius and length of the pore to be $R = 1^{-}\mathrm{m}$ and $L = 10^{-}\mathrm{m}$, respectively (Nelson 2009). We find that the velocity of the oil slug increases as the salinity decreases, which is consistent with the proposed mechanisms. The velocity increases by 30% for the MIE mechanism and 20% for the local and global pH increase mechanisms. At high-salinities, a different model needs to be considered since the thin water film is not present between the oil and clay. However, an alternative model is beyond the scope of this paper, and in practice, structural forces will prevent the film thickness from decreasing to zero. In Fig. 12b, we plot the speed of the oil slug, $V$, against the salinity parameter, $\tau$, for the case in which the surface area of the clay is high, $A_c = 2\pi \times 10^{-9}\,\mathrm{m}^2$. We observe that the MIE and local pH increase mechanisms are unaffected by the change in the surface area (in comparison with Fig. 12a), but that the increase in the speed of the oil slug as the salinity decreases is greater for the global pH increase mechanism.

Following the methodology outlined in this paper, it is possible to study alternative reaction-based LSW models by first using a law-of-mass-action approach to determine the charges on the oil and clay surfaces, then substituting these expressions into (23) to find the film thickness, and, finally, substituting this into (29) to find the velocity of the oil. If the LSE is the result of an increase in the relative permeability of the oil phase, which in turn is the result of an increase in the oil mobility, then studying alternative models could be useful for determining the dominant mechanism, and, potentially, optimising a low-salinity injection.

## 5 Conclusions and Discussion

In this paper, we built models to investigate the effect of multicomponent ionic exchange and pH increase (both local and global) on low-salinity waterflooding. We considered the canonical problem of a charged oil surface separated from a charged clay pore wall by a layer of brine. We derived expressions, (3), (4), (10), and (12), for the surface charge densities on the two surfaces. We simplified the three-particle interactions in the MIE, local pH increase, and global pH increase mechanisms by treating each charged surface separately. Improvements to the model could be made by considering three-particle interactions; however, the mean-field assumption required to apply the Poisson–Boltzmann equation no longer applies in this instance, and a more complicated model would be required.

Our numerical results indicate that, for all three mechanisms, the surface charge reduces during a low-salinity waterflood as a result of cation desorption on the oil and mineral surfaces; this reduction is often described as being the cause of the LSE. An increase in the

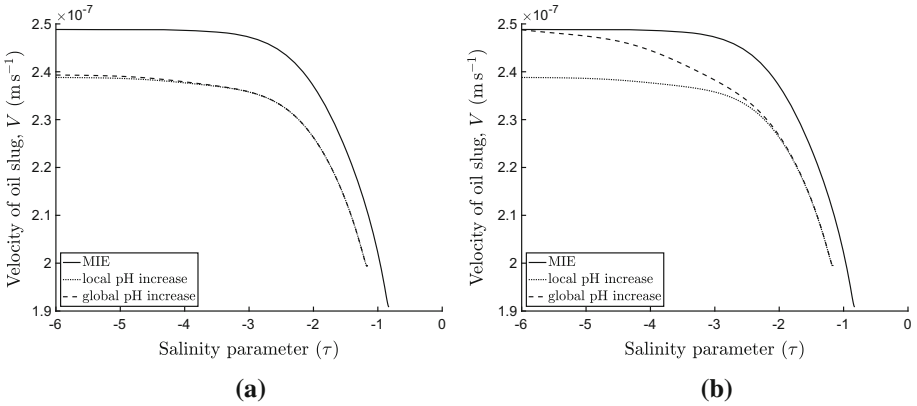


**Fig. 12** **a** Velocity of the oil slug as a function of the salinity of the surrounding brine, for the MIE, local pH increase, and global pH increase mechanisms. The parameter values are given in Table 1. **b** Velocity of the oil slug as a function of the salinity of the surrounding brine for the three mechanisms for the $A_c = 2\pi \times 10^{-9}$ m$^2$ case

pH is not observed in the local pH increase mechanism. However, by extending the model to allow global variations in the pH, we were able to produce this effect. We observed that the surface charge of the oil phase is sensitive to the surface area of the clay in the global pH increase mechanism, but not in the MIE and local pH increase mechanisms, which may help to distinguish the mechanisms experimentally. To explore these models further, instead of separating the processes to determine the dominant mechanism, the reactions from each mechanism may be combined into a single model, so that the dominant terms for a given system can be determined using the relevant parameters for the particular clays and oils being studied.

Using the expressions for the surface charge densities of the oil and clay surfaces obtained from the three reaction models, we derived an expression [Eq. (21)] for the electrostatic component of the disjoining pressure acting between a static oil–water interface and a clay surface. The total disjoining pressure was then found by combining this with the contribution due to van der Waals forces. By balancing the total disjoining pressure with the capillary pressure across the oil–water interface, we were able to derive an expression [Eq. (23)] for the equilibrium film thickness of the water film separating the oil from the clay. We observed that, as the salinity of the brine reduces, the thickness of the film increases. This is due to a combination of electric double layer expansion, and the increased repulsion between the oil and clay as a result of the reactions occurring on the two surfaces. This is consistent with the conclusions of Austad et al. (2010) and Lager et al. (2008), and experiments conducted by Lee et al. (2010), in which the film thickness was directly measured using small angle neutron scattering.

We also observed that, as the salinity increases, the film thickness reduces to zero when van der Waals forces are included. However, for films $\mathcal{O}(10^{-10}\text{m})$ or less, the finite size of the ions becomes important, and structural forces need to be included in the model. With these forces included, the film thickness is always positive; Hirasaki (1991) discusses this issue in more detail.

We proposed the theory that an increase in the film thickness on the pore scale results in greater oil recovery on the core scale since the increased film thickness allows oil to slide along the clay surface, with the wetting film acting as a slip layer. This increases the mobility

of the oil slug on the pore scale, which results in an increase in the relative permeability of the oil phase on the macroscopic scale. To explore this idea, we studied the motion of an oil slug through a pore, under the action of an applied pressure difference. We present Eq. (26) for the film thickness below the oil slug and observed that the film thickness is approximately the same as for a static oil droplet for pressures typically observed in an oil reservoir, since the oil slug is moving sufficiently slowly.

Having determined the film thickness, $h^*$, we present expression (29) for the velocity of oil slug, $V$, as a function of $h^*$. By plotting the velocity of the oil slug against the salinity, we found that, for the MIE, local pH increase, and global pH increase mechanisms, the velocity increases by approximately 30% and 20%, respectively, during a low-salinity waterflood. However, these values are dependent on the type of clay being studied, the size of the oil slug, the size of the pore, the viscosity of the oil, and the dissociation constants used for the reactions occurring on the oil and clay surfaces. Hence, the exact values will vary for different systems.

Despite the number of simplifying assumptions we have made, the model we have presented in this paper is able to capture some of the phenomena observed during a low-salinity waterflood. However, our model neglects a number of important salinity-dependent effects such as pinning/de-pinning of the contact line (Brady et al. 2015; Schmatz et al. 2015), and variations in the surface rheology of the oil–water interface (Alvarado et al. 2014b; Garcia-Olvera et al. 2016). Extending the model in this manner will be required in order to understand some of the key phenomenology observed experimentally, such as phase-trapping and pinning. The model we have presented is the first step towards developing a comprehensive pore-scale model in which these additional phenomenological effects may be captured.

To study the effect of the increased oil mobility, and whether this leads to greater oil recovery, a macroscopic model of LSW is needed. The aim of future work is to derive such a model using a combination of network modelling and homogenisation. With a larger-scale model, the theory can be directly compared with core-scale experiments, to determine whether increased slip due to cation exchange accurately predicts the effect of a low-salinity injection. With the method presented here, it is straightforward to study the effect of different reactions occurring on the clay surface, by deriving expressions for the surface charge densities, and substituting them into the expressions for the film thickness and velocity. Hence, alternative mechanisms can be easily compared, providing an alternative approach to core-scale experiments as a way of determining the dominant causal mechanism.

**Acknowledgements** We would like to thank BP and EPSRC for providing funding for this research in the form of a CASE award, Grant Number EP/M50659X/1. We would also like to thank Bilal Rashid, Tim Totton, and Pete Salino for their invaluable guidance on the industrial aspects of this work.



## References

Alvarado, V., Garcia-Olvera, G., Hoyer, P., Lehmann, T.E., et al.: Impact of polar components on crude oil–water interfacial film formation: a mechanisms for low-salinity waterflooding. In: SPE Annual Technical Conference and Exhibition. Society of Petroleum Engineers (2014a)

Alvarado, V., Moradi Bidhendi, M., Garcia-Olvera, G., Morin, B., Oakey, J.S., et al.: Interfacial visco-elasticity of crude oil-brine: an alternative EOR mechanism in smart waterflooding. In: SPE Improved Oil Recovery Symposium. Society of Petroleum Engineers (2014b)
Andelman, D.: Electrostatic properties of membranes: the Poisson–Boltzmann theory. Handb. Biol. Phys. **1**, 603–642 (1995)
Austad, T., RezaeiDoust, A., Puntervold, T.: Chemical mechanism of low salinity water flooding in sandstone reservoirs. In: SPE Improved Oil Recovery Symposium. Society of Petroleum Engineers (2010)
Bahrami, M., Tamayol, A., Taheri, P.: Slip-flow pressure drop in microchannels of general cross section. J. Fluids Eng. **131**(3), 031201 (2009)
Bartels, W.B., Mahani, H., Berg, S., Menezes, R., van der Hoeven, J.A., Fadili, A., et al.: Oil configuration under high-salinity and low-salinity conditions at pore scale: a parametric investigation by use of a single-channel micromodel. SPE J. **22**(05), 1–362 (2017)
Ben-Yaakov, D., Andelman, D.: Revisiting the Poisson–Boltzmann theory: charge surfaces, multivalent ions and inter-plate forces. Phys. A Stat. Mech. Appl. **389**(15), 2956–2961 (2010)
Brady, P.V., Morrow, N.R., Fogden, A., Deniz, V., Loahardjo, N.: Electrostatics and the low salinity effect in sandstone reservoirs. Energy Fuels **29**(2), 666–677 (2015)
Buckley, J.S.: Mechanisms and consequences of wettability alteration by crude oils. Ph.D. thesis, Heriot-Watt University (1996)
Derjaguin, B.V., Landau, L.: Theory of the stability of strongly charged lyophobic sols and of the adhesion of strongly charged particles in solutions of electrolytes. Acta Physicochim. URSS **14**(6), 633–662 (1941)
Drummond, C., Israelachvili, J.: Fundamental studies of crude oil-surface water interactions and its relationship to reservoir wettability. J. Pet. Sci. Eng. **45**(1), 61–81 (2004)
Eslinger, E., Pevear, D.: Clay minerals for petroleum geologists and engineers. Society of Economic Paleontologists and Mineralogists (1988)
Fletcher, P., Sposito, G.: Chemical modeling of clay/electrolyte interactions of montmorillonite. Clay Miner. **24**(2), 375–391 (1989)
Fournier, P., Oelkers, E.H., Gout, R., Pokrovski, G.: Experimental determination of aqueous sodium-acetate dissociation constants at temperatures from 20 to 240 C. Chem. Geol. **151**(1), 69–84 (1998)
Garcia-Olvera, G., Reilly, T.M., Lehmann, T.E., Alvarado, V.: Effects of asphaltenes and organic acids on crude oil-brine interfacial visco-elasticity and oil recovery in low-salinity waterflooding. Fuel **185**, 151–163 (2016)
Ghosal, S.: Lubrication theory for electro-osmotic flow in a microfluidic channel of slowly varying cross-section and wall charge. J. Fluid Mech. **459**, 103–128 (2002)
Hadia, N.J., Hansen, T., Tweheyo, M.T., Torsæter, O.: Influence of crude oil components on recovery by high and low salinity waterflooding. Energy Fuels **26**(7), 4328–4335 (2012)
Hang, P.T., Brindley, G.W.: Methylene blue absorption by clay minerals. Determination of surface areas and cation exchange capacities (clay-organic studies XVIII). Clays Clay Miner. **18**(4), 203–212 (1970)
Hilner, E., Andersson, M.P., Hassenkam, T., Matthiesen, J., Salino, P.A., Stipp, S.L.S.: The effect of ionic strength on oil adhesion in sandstone-the search for the low salinity mechanism. Sci. Rep. **5**, 9933 (2015)
Hirasaki, G.: Wettability: fundamentals and surface forces. SPE Form. Eval. **6**(02), 217–226 (1991)
Jadhunandan, P.: Effects of brine composition, crude oil, and aging conditions on wettability and oil recovery. Ph.D. thesis, Department of Petroleum Engineering, New Mexico Institute of Mining & Technology (1990)
Joseph, N.R.: The dissociation constants of organic calcium complexes. J. Biol. Chem. **164**(2), 529–541 (1946)
Kawaguchi, S., Yekta, A., Winnik, M.A.: Surface characterization and dissociation properties of carboxylic acid core-shell latex particle by potentiometric and conductometric titration. J. Colloid Interface Sci. **176**(2), 362–369 (1995)
Kovscek, A., Wong, H., Radke, C.: A pore-level scenario for the development of mixed wettability in oil reservoirs. AIChE J. **39**(6), 1072–1085 (1993)
Kütt, A., Leito, I., Kaljurand, I., Sooväli, L., Vlasov, V.M., Yagupolskii, L.M., Koppel, I.A.: A comprehensive self-consistent spectrophotometric acidity scale of neutral brønsted acids in acetonitrile. J. Org. Chem. **71**(7), 2829–2838 (2006)
Lager, A., Webb, K., Black, C., Singleton, M., Sorbie, K.: Low salinity oil recovery—an experimental investigation. Petrophysics **49**(1), 28–35 (2008)
Lee, S., Webb, K., Collins, I., Lager, A., Clarke, S., O'Sullivan, M., Routh, A., Wang, X.: Low salinity oil recovery: increasing understanding of the underlying mechanisms. In: SPE Improved Oil Recovery Symposium. Society of Petroleum Engineers (2010)
Lewis, W.C.M.: The electric charge at an oil–water interface. Trans. Faraday Soc. **33**, 708–713 (1937)

Ligthelm, D.J., Gronsveld, J., Hofman, J., Brussee, N., Marcelis, F., van der Linde, H.: Novel waterflooding strategy by manipulation of injection brine composition. In: EUROPEC/EAGE Conference and Exhibition. Society of Petroleum Engineers (2009)
Liu, X., Lu, X., Sprik, M., Cheng, J., Meijer, E.J., Wang, R.: Acidity of edge surface sites of montmorillonite and kaolinite. Geochim. Cosmochim. Acta **117**, 180–190 (2013)
Mahani, H., Berg, S., Ilic, D., Bartels, W.B., Joekar-Niasar, V., et al.: Kinetics of low-salinity-flooding effect. SPE J. **20**(01), 8–20 (2015)
Malmberg, C.G., Maryott, A.A.: Dielectric constant of water from 00 to 1000 C. J. Res. Nat. Bureau Stand. **56**, 1–8 (1956)
Masliyah, J.H., Bhattacharjee, S.: Electrokinetic and Colloid Transport Phenomena. Wiley, Hoboken (2006)
McCormack, D., Carnie, S., Chan, D.: Calculations of electric double-layer force and interaction free energy between dissimilar surfaces. J. Colloid Interface Sci. **169**(1), 177–196 (1995)
McGuire, P.L., Chatham, J.R., Paskvan, F.K., Sommer, D.M., Carini, F.H.: Low salinity oil recovery: an exciting new EOR opportunity for Alaska's north slope. In: SPE Western Regional Meeting. Society of Petroleum Engineers (2005)
Moradi, M., Alvarado, V., Huzurbazar, S.: Effect of salinity on water-in-crude oil emulsion: evaluation through drop-size distribution proxy. Energy Fuels **25**(1), 260–268 (2010)
Nasralla, R.A., Bataweel, M.A., Nasr-El-Din, H.A., et al.: Investigation of wettability alteration and oil-recovery improvement by low-salinity water in sandstone rock. J. Can. Pet. Technol. **52**(02), 144–154 (2013)
Nasralla, R.A., Nasr-El-Din, H.A., et al.: Double-layer expansion: is it a primary mechanism of improved oil recovery by low-salinity waterflooding? SPE Reserv. Eval. Eng. **17**(01), 49–59 (2014)
Nelson, P.: Pore-throat sizes in sandstones, tight sandstones, and shales. AAPG Bull. **93**(3), 329–340 (2009)
Ohshima, H.: Diffuse double layer interaction between two parallel plates with constant surface charge density in an electrolyte solution i. Colloid Polym. Sci. **252**(3), 158–164 (1974a)
Ohshima, H.: Diffuse double layer interaction between two parallel plates with constant surface charge density in an electrolyte solution ii. Colloid Polym. Sci. **252**(3), 257–267 (1974b)
Parsegian, V., Gingell, D.: On the electrostatic interaction across a salt solution between two bodies bearing unequal charges. Biophys. J. **12**(9), 1192–1204 (1972)
Raeesi, B., Morrow, N.R., Mason, G.: Effect of surface roughness on wettability and displacement curvature in tubes of uniform cross-section. Colloids Surf. A Physicochem. Eng. Asp. **436**, 392–401 (2013)
RezaeiDoust, A., Puntervold, T., Austad, T.: Chemical verification of the eor mechanism by using low saline/smart water in sandstone. Energy Fuels **25**(5), 2151–2162 (2011)
Schmatz, J., Urai, J.L., Berg, S., Ott, H.: Nanoscale imaging of pore-scale fluid–fluid–solid contacts in sandstone. Geophys. Res. Lett. **42**(7), 2189–2195 (2015)
Tang, G.Q., Morrow, N.R.: Effect of temperature, salinity and oil composition on wetting behavior and oil recovery by waterflooding. Technical report, Society of Petroleum Engineers (SPE), Inc., Richardson, TX, USA (1996)
Tang, G.Q., Morrow, N.R.: Influence of brine composition and fines migration on crude oil/brine/rock interactions and oil recovery. J. Pet. Sci. Eng. **24**(2), 99–111 (1999)
Tehan, B.G., Lloyd, E.J., Wong, M.G., Pitt, W.R., Montana, J.G., Manallack, D.T., Gancia, E.: Estimation of PKA using semiempirical molecular orbital methods. Part 1: application to phenols and carboxylic acids. Mol. Inform. **21**(5), 457–472 (2002)
Verwey, E.J.W., Overbeek, J.T.G.: Theory of the Stability of Lyophobic Colloids. Elsevier, Amsterdam (1948)
Wang, X., Alvarado, V.: Effects of aqueous-phase salinity on water-in-crude oil emulsion stability. J. Dispers. Sci. Technol. **33**(2), 165–170 (2012)
Wilmott, Z.M., Breward, C.J.W., Chapman, S.J.: Slip flow through channels with varying elliptic cross section. IMA J. Appl. Math. **83**(5), 874–893 (2018a)
Wilmott, Z.M., Breward, C.J.W., Chapman, S.J.: The effect of ions on the motion of an oil slug through a charged capillary. J. Fluid Mech. **841**, 310–350 (2018b)
Wong, H., Morris, S., Radke, C.: Three-dimensional menisci in polygonal capillaries. J. Colloid Interface Sci. **148**(2), 317–336 (1992)
Xiao, L., Cai, Q., Ye, X., Wang, J., Luo, R.: Electrostatic forces in the Poisson–Boltzmann systems. J. Chem. Phys. **139**(9), 09B627-1 (2013)
Yildiz, H., Morrow, N.R.: Effect of brine composition on recovery of Moutray crude oil by waterflooding. J. Pet. Sci. Eng. **14**(3), 159–168 (1996)